J. Astrophys. Astr. (1999) **20**, 23-35

Infrared Emission from Interstellar Dust Cloud with Two Embedded Sources: IRAS 19181 + 1349

A. D. Karnik & S. K. Ghosh, *Tata Institute of Fundamental Research, Homi Bhabha Road, Colaba, Mumbai (Bombay) 400 005, India.*

Received 1999 June 18; accepted 1999 June 30

Abstract. Mid- and far-infrared maps of many Galactic star forming regions show multiple peaks in close proximity, implying more than one embedded energy source. With the aim of understanding such interstellar clouds better, the present study models the case of two embedded sources. A radiative transfer scheme has been developed to deal with a uniform density dust cloud in a cylindrical geometry, which includes isotropic scattering in addition to the emission and absorption processes. This scheme has been applied to the Galactic star forming region associated with IRAS 19181 + 1349, which shows observational evidence for two embedded energy sources. Two independent modelling approaches have been adopted, viz., to fit the observed spectral energy distribution (SED) best; or to fit the various radial profiles best, as a function of wavelength. Both the models imply remarkably similar physical parameters.

Key words. Interstellar clouds—infrared SED—IRAS 19181 + 1349.

1. Introduction

Galactic star forming regions mostly comprise of Young Stellar Objects (YSOs)/ protostars still buried inside/in the vicinity of the parent interstellar cloud from which they are formed. Hence the study of YSOs leads to understanding of the interstellar medium in the close neighborhood of the starbirth. Early evolution of star forming regions is obviously more important from the point of understanding the star formation process itself. Typically the photons from the embedded energy source, protostar/ZAMS star, get reprocessed by the dust component of the interstellar medium in the immediate neighborhood. The dust grains absorb/scatter the incident radiation, depending on their dielectric properties. The dust grains acquire an equilibrium temperature based on the local radiation field which depends on the distance from the energy source and secondary radiation from other grains. The reradiation from the grains in the outer regions, is what is observable. Hence, the emerging observable spectrum can in principle be connected to the spectrum of the embedded protostar/ZAMS star through detailed radiation transfer provided some details about the geometry are known.

In order to study the earliest stage of star formation, a large amount of observational effort is directed towards far infrared / sub-mm observations of prospective young star forming regions. Many Galactic star forming regions have been mapped with near diffraction limited angular resolutions, using Kuiper Airborne Observatory,

Infrared Space Observatory (ISO), James Clerk Maxwell Telescope etc. in recent times. In many cases, the maps of continuum emission resolve several closeby individual intensity peaks as evident from the morphology of their isophots.

The present study is a step in the direction of extracting maximum possible information about the geometrical and physical details of the source by comparing radiative transfer models with observations in cases where two nearby sources are resolved. Here, the "nearby" implies the interference in energetics of each of the two resolved sources by the other one. The heating of dust in a cloud with multiple sources has been studied by Rouan (1979) under certain simplification. However, the problem of more than one embedded source has rarely been addressed quantitatively. The existing observational data showing clear evidence of resolved multiple embedded sources justify the need to explore geometries dealing with more than one embedded source. Ghosh & Tandon (1985) attempted to study the case of two embedded sources with many simplifying assumptions. They neglected some basic phenomena like scattering which limited its applicability to $\lambda \geq 50$ μm only. The present work is an extension of this earlier attempt by including the effect of isotropic scattering.

In section 2 the problem has been formulated and the radiation transfer scheme is described. In section 3, we model observations of IRAS 19181 + 1349 which shows evidence of having two embedded sources. The results of our modelling are then discussed.

2. Model formulation

The primary aim of the present model is to reproduce the infrared emission from a star forming cloud with two embedded sources, keeping the computational complexities at a minimum level.

The interstellar cloud is assumed to be of cylindrical shape. As a starting point, a uniform density of the cloud has been assumed. The line joining the two embedded ZAMS stellar/ protostellar energy sources defines the symmetry axis of the problem. Around each of the sources there will be a dust free cavity (Fig. 1). The existence of such a cavity is widely accepted due to evaporation of the dust grains in the intense radiation field. In addition, radiation pressure effects on the dust grains may also play a role in deciding the cavity size. The radiation transfer is carried out through the dust component alone. Dust grains with a continuous size distribution have been considered, and their composition is a parameter of modelling. Three types of grains, viz., Graphite, Astronomical Silicate and Silicon Carbide have been invoked since their existence is generally accepted. All properties of the dust grains, viz., absorption and scattering coefficients as a function of wavelength, for various sizes and all three types of grains, have been taken from Laor & Draine (1993). The size distribution of all the three types of grains has been assumed to be power law ($n(a)\mathrm{d}a \sim a^{-3.5}\mathrm{d}a$) as per Mathis, Rumpl & Nordsieck (1977). The wavelength grid used 89 points covering from the Lyman continuum limit to the millimeter wavelengths.

The geometrical parameters relevant to the model (Fig. 1) include the radius of the cylinder (R_{cyl}), radii of dust free cavities near the two sources (R_{c1}, R_{c2}), and distance between two exciting sources (D). Other physical parameters are the composition of the dust (relative abundances of three types of dust components) and the dust density expressed in optical depth at 100 μm (τ_{100}). The optical depth at any other wavelength

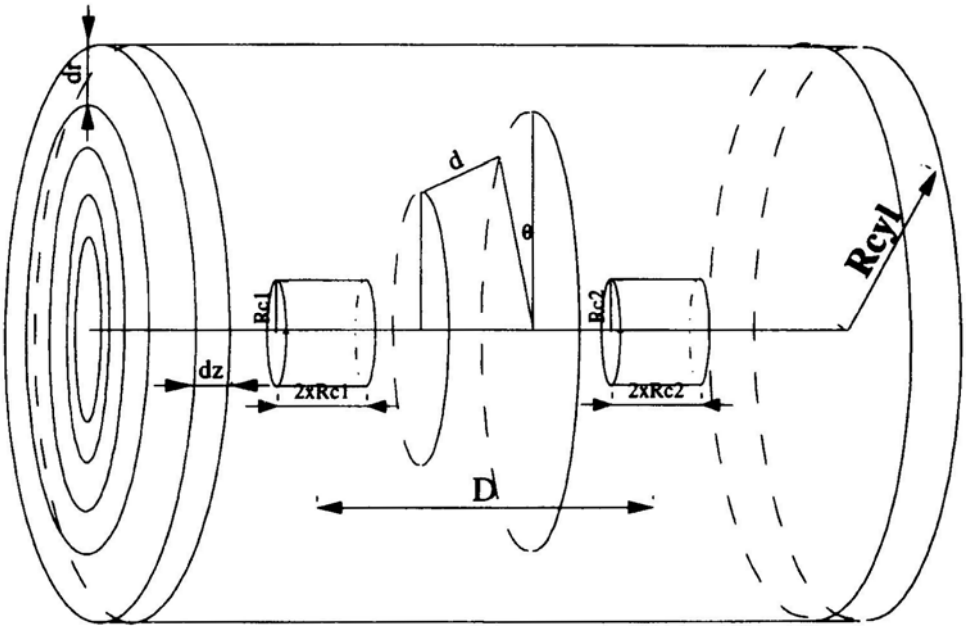

Figure 1. The geometry of the cylindrical cloud considered in the present study. The embedded energy sources lie along the axis of the cylinder (at the centers of the two small cylinders) separated by distance *D*. The two small cylinders represent the dust free cavities near the respective sources. The *z*-axis is defined to be along the symmetry axis of the cylinder. The cloud is divided into n_z disks along z-axis, and each disk into n_r concentric rings.

is uniquely connected to τ_{100} via the dust properties and composition assumed in the particular model. The cylindrical interstellar cloud is divided into n_z identical discs. Each of these discs is further divided into n_r annular rings. The n_z is chosen such that each disc is optically thin even at UV, along the *z*-axis. Along the radial direction (total number of grid points being n_r), a two stage grid has been employed which is initially nearly logarithmically spaced (near the symmetry axis) and linearly spaced in the outer regions of the cylinder. This scheme of radial grid has been arrived at by keeping the optical depth related inaccuracies under check, for the entire wavelength region considered for the radiation transfer. Both the near logarithmic and the linear grids are matched by ensuring that radial cell size, $\delta r(n_r)$, is a smooth function of n_r. For modelling attempts of IRAS 19181 + 1349 a grid of 600 points in axial direction and of 25 points in radial direction were employed.

The relevant calculations are represented in equations (l)–(7). For clarity the frequency suffix has been dropped from all the terms, though calculations are performed for each frequency grid point. The quantities in angled brackets are averages over the dust size distribution. The code is simplified and optimized in many ways in view of the memory requirements and speed. Initially, factors totally dependent on the geometry of the problem and which do not change in each iteration are calculated. These include the optical depth terms and the geometric integrals involved in computations of radiation received by a unit volume element of the ring *i* from the ring *j* (equation (1)). The geometric symmetry is such that such terms only depend on the axial separation between the two rings and their respective radii. The

total flux absorbed and scattered by unit volume in each ring due to radiation from other rings is then calculated (equation (2)). Also, the radiation received by a unit volume element of the ring i from embedded sources depends only on the geometry and the optical depth per unit length of the particular model and hence is fixed over iterations (equation (3)). The equilibrium temperature of the dust grains (on the median circle) for any particular annular ring is calculated using an iterative scheme by equating the power radiated by the dust (equation (6)) to the power absorbed (equation(7)). The latter is contributed by the embedded exciting sources (attenuated by the line of sight dust) as well as secondary emission and scattering from dust grains in all other annular rings (equation (4)). This simplifies the calculations leading to a set of coupled equations with only two parameters per ring, temperature (T_i) and F^i changing from iteration to iteration thus greatly reducing the memory requirements.

$$F_r^{i,j} = \sum_{\theta} \frac{e^{-\langle \pi a^2 Q_{\text{ext}} \rangle n_d d_{i,j,\theta}}}{d_{i,j,\theta}^2} \left[\langle \pi a^2 Q_{\text{abs}} \rangle n_d B(T_j) + \frac{\langle \pi a^2 Q_{\text{scat}} \rangle F^j}{4\pi \langle \pi a^2 Q_{\text{ext}} \rangle} \right] \Delta r_j \, \Delta z \, \Delta\theta r_j, \tag{1}$$

$$F_r^i = \sum_{j=1, j\neq i}^{n_r \times n_z} \langle \pi a^2 Q_{\text{ext}} \rangle n_d F_r^{i,j}, \tag{2}$$

$$F_s^i = \sum_{s=1}^{2} \langle \pi a^2 Q_{\text{ext}} \rangle \frac{\pi R_s^2 F_s}{r_{i,s}^2} e^{-\langle \pi a^2 Q_{\text{ext}} \rangle n_d (r_{i,s} - r_{c,s})}, \tag{3}$$

$$F^i = F_r^i + F_s^i, \tag{4}$$

$$F_e^i = \langle \pi a^2 Q_{\text{abs}} \rangle 4\pi B(T_i), \tag{5}$$

$$P_{\text{Emitted}} = \int F_e^i d\nu, \tag{6}$$

$$P_{\text{Absorbed}} = \int \frac{\langle \pi a^2 Q_{\text{abs}} \rangle}{\langle \pi a^2 Q_{\text{ext}} \rangle} (F_r^i + F_s^i) d\nu, \tag{7}$$

Where

$d^2 \equiv (z_i - z_j)^2 + (r_i)^2 + (r_j)^2 - 2 r_i r_j \cos(\theta)$
θ is azimuthal angular difference between two volume unit under consideration.
$r_{i,s}^2 \equiv (z_i - z_s)^2 + r_i^2$
$r_{c,s}^2 \equiv$ dust cavity radius for source s.
$Q_{\text{ext}} \equiv Q_{\text{abs}} + Q_{\text{scat}}$
$n_d \equiv$ number density of dust grains.
$T_i \equiv$ Temperature of dust in ring i.
$F_s \equiv$ surface flux spectrum for source s.
$F_r^i \equiv$ Flux absorbed and scattered by unit volume of ring i, due to other rings.
$F_s^i \equiv$ Flux absorbed and scattered by unit volume of ring i, due to sources.
$F^i \equiv$ Total flux absorbed and scattered by unit volume of ring i.
$B(T) \equiv$ Planck function.

The dust temperature for each annular ring, leading to the temperature distribution throughout the cloud, is determined iteratively. Initially (the very first iteration), only

the two embedded sources power the heating of the grains. From the second iteration onwards the effects of secondary heating and scattering are taken into account. In this iterative procedure the temperature of each annular ring is gradually updated in each iteration satisfying the condition $P_{\text{Emitted}} = P_{\text{Absorbed}}$. The iterations are continued till the fractional changes in absorbed power for each annular ring, between successive iterations, reduces below the convergence criteria.

The emergent intensity distribution, as seen by a distant observer is predicted by integrating the emitted and scattered radiation along relevant lines of sight and taking account of extinction due to the line of sight optical depth. This spatial intensity distribution at any selected wavelength is convolved with the relevant instrumental beam profile (PSF) for direct comparison with observations.

Before applying the scheme developed above to any astrophysical source it is necessary to verify its reliability and quantify its accuracy. For this, we simulate the case of a single embedded source by "dimming" one of the two sources thereby keeping our original code intact during the test runs. This simulates a single exciting source embedded on the symmetry axis of the uniform density cylindrically shaped cloud. The size of the cylindrical cloud has been chosen such that the results from other codes using spherically symmetric geometry could be compared effectively. We have used the well established code CSDUST3 (Egan, Leung & Spagna 1988) for such a comparison.

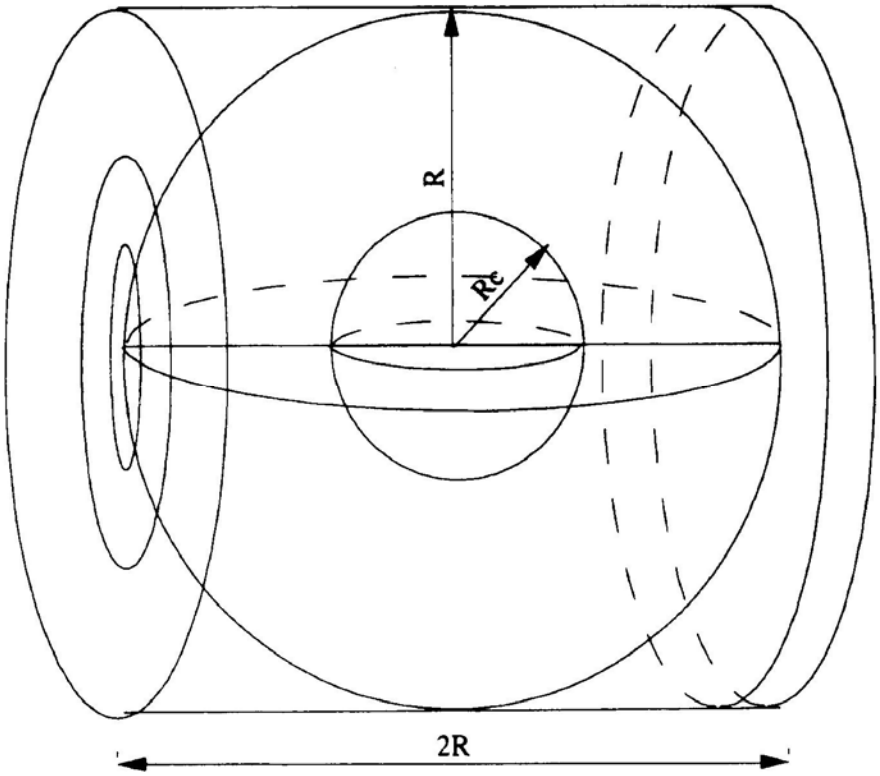

Figure 2. The geometrical dimensions of the spherical (CSDUST3) and the cylindrical modelling schemes under comparison.

The radius of the cylindrical cloud used for comparing our code with the spherically symmetric code was identical to that of the "equivalent" spherical cloud. The length of the cylinder (along z-axis) is twice this radius. Fig. 2 is a schematic of the cylindrical as well as the spherical models.

The assumed radius of the cylinder, as well as the sphere, was 2 pc. The radius of the dust free cavity near the source was adopted to be .01 pc. In order to make the comparison possible and effective, all model parameters were made identical for both the codes. These include: dust size distribution; dust number density (and hence total optical depth along the line of sight between the embedded source and the distant observer). A typical dust composition has been assumed consisting of 50 % Graphite and 50 % Astronomical Silicate. The embedded energy source was assumed to be a single ZAMS 05 star with luminosity $9.0 \times 10^5 L_{\odot}$. Some parameters were explored (e.g. optical depth) to study regions of validity with specified accuracy, by changing them identically for both the schemes. A large range in the optical depth τ_{100},viz., 1.0×10^{-3} to 0.1 was covered during the test runs.

The comparison of the emergent spectral energy distributions (SEDs) from both the schemes for various optical depths are shown in Fig. 3. It may be seen that the SEDs match quantitatively over a wide range of optical depths from mid-infrared to millimeter wavelengths. There are some differences at near infrared wavelengths; this is to be expected from the differences in the cell sizes and the geometry. However, since the main motive of the present study is to interpret measurements in the wavebands beyond the mid-IR, our code may be considered to be satisfactory. From this comparative study we conclude that our code is accurate up to an optical depth corresponding to $\tau_{100} \approx 0.06$ ($\tau_{1\ \mu m} \approx 6$), for the present choice of grid points. This limit already corresponds to much denser clouds than generally found in the Galactic star forming regions.

3. IRAS 19181 +1349

The Galactic star forming region IRAS 19181 + 1349 is an IRAS Point Source Catalog (IRAS PSC) source associated with the radio source G48.60 + 00. The presence of a radio continuum suggests ongoing high mass star formation in the region. This source has been resolved in two components in the 210 μm map (Fig. 4b) generated from the observations using the TIFR 1-meter balloon borne telescope (Karnik *et al.* 1999). Although a single IRAS PSC source is associated with this star forming region, the HIRES processing of the IRAS survey data has led to the resolution of these two sources in the 12 and 25 μm band maps. The map at 12 μm is shown in Fig. 4(a). We denote FIR peak with higher R.A. as S1 and that of lower R.A. S2, respectively, hereafter. Zoonematkermani *et al.* (1990) have reported four compact radio sources 48.603 + 0.026, 48.609 + 0.027, 48.606 + 0.023 and 48.592 + 0.044 in this region. The first three of these closely match S1 (positionally) while the fourth one matches S2. Kurtz, Churchwell & Wood (1994) have also reported three ultracompact HII regions which are positionally close to S1, indicating ongoing high mass star formation in a very early evolutionary phase. This source has also been observed using the ISOCAM instrument onboard Infrared Space Observatory (ISO) using seven filters centred at four PAH features and 3 continuua (3.30, 3.72, 6.00, 6.75, 7.75, 9.63, 11.37 μm; Verma *et al.* 1999). The ISOCAM images at all the bands

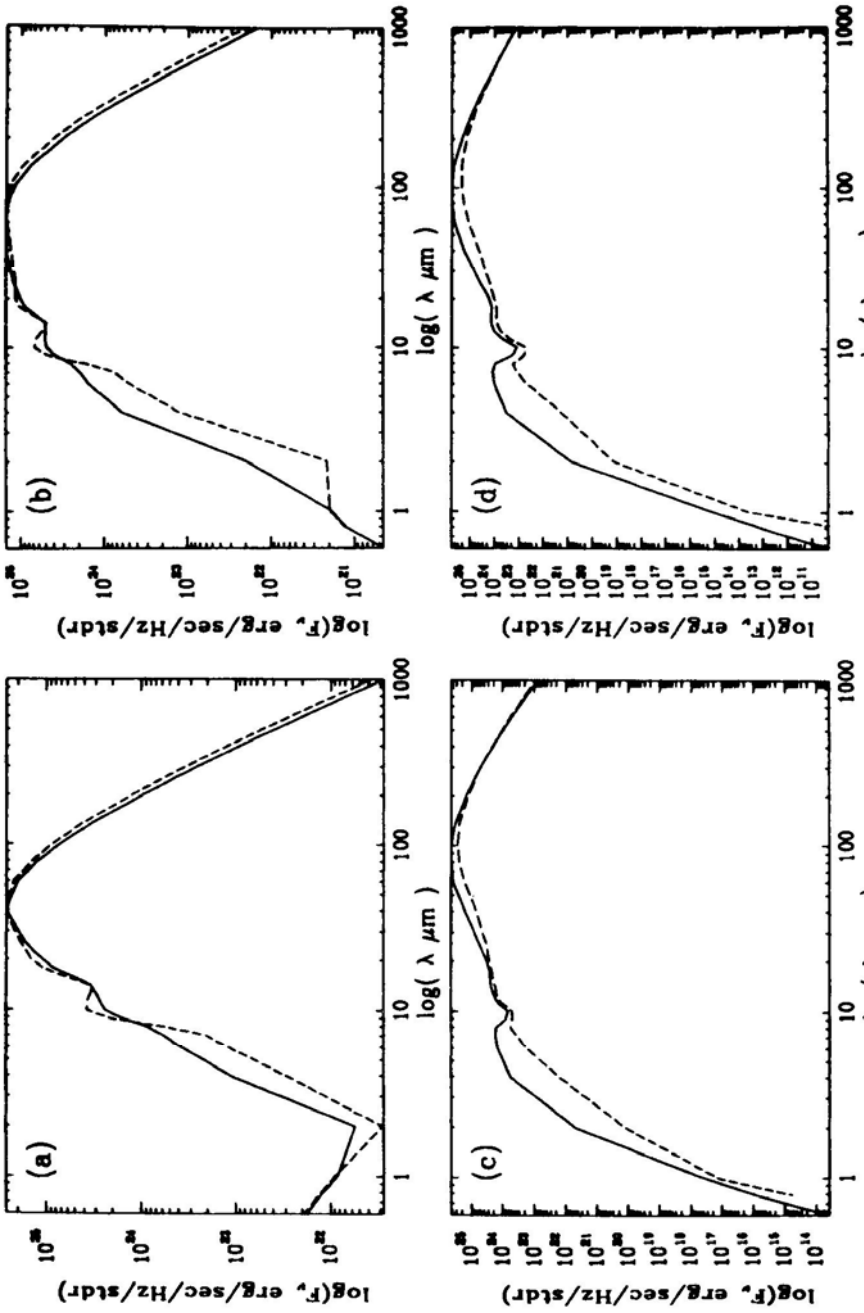

Figure 3. The comparison of predicted SEDs from the two schemes. The continuous lines represent CSDUST3 while the dashed lines refer to our scheme. The SEDs correspond to τ_{100} of – (**a**) 0.001, (**b**) .01, (**c**) .06 and (**d**) 0.1.

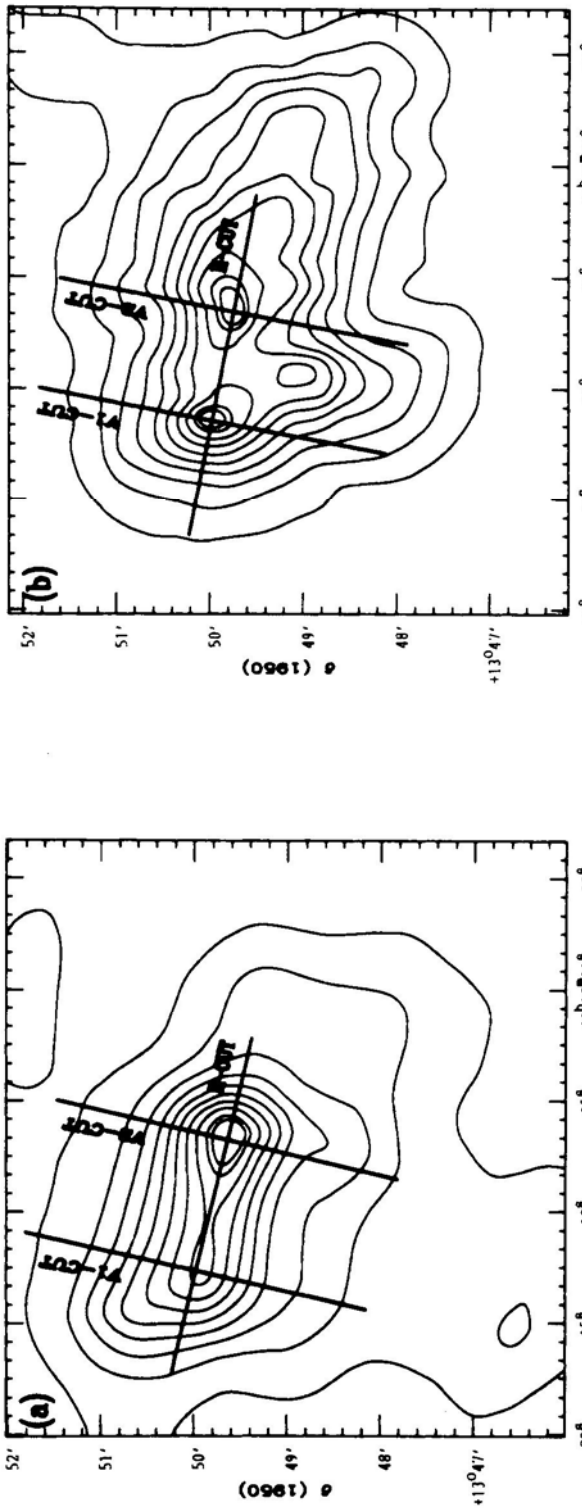

Figure 4. The infrared maps of IRAS 19181 + 1349 at (**a**) 12 μm and (**b**) 210 μm. Contours are drawn at 10, 20, 30, 40, 50, 60, 70, 80, 90, 95 per cent of peak intensities 26 and 303 Jy/(arc min)^2 respectively. The straight lines show the positions of radial and axial cuts compared with the model in Fig.6.

show two extended prominent complexes with multiple peaks. Hence from radio as well as mid to far infrared observations the nature of IRAS 19181 + 1349 is established to be of double embedded source/cluster type.

This seems to be an ideal astrophysical example of interstellar cloud with two embedded sources. We attempt to model this source with our scheme to extract important physical parameters about the embedded energy sources as well as the intervening interstellar medium in IRAS 19181 + 1349. Next we describe the results obtained from such a study.

The source IRAS 19181 + 1349 was considered as a cylindrical dust cloud with two protostellar/ZAMS stellar sources embedded along the axis of the cylinder. The size of the cloud and the dust density were used as free parameters. The sum of the luminosities of the two embedded sources is determined by integrating the observed spectral energy distribution (SED). The observations used for this integration includes the four IRAS bands and the two TIFR bands. This total luminosity is treated as an observational constraint in the modelling. Further observational constraints include: the shape of the SED which was obtained from HIRES-IRAS, TIFR and ISO observations, and the structural morphology of IRAS 19181+1349 as reflected by the isophote contours of the high angular resolution maps at 12 and 210 μm. As our code does not deal with the physics of PAH emission at present, only the data in ISOCAM filters sampling the continuua have been used to constrain the model.

Two completely independent approaches have been followed in modelling IRAS 19181 + 1349 using our scheme. In each approach, all the model parameters are floated to obtain the best fit model. The parameters fine tuned to achieve the best fit model are: luminosities of individual embedded sources; geometrical size details of the cylindrical cloud (including the size of the cavity); and the dust density/optical depth. The main aim of the first approach is to optimize the fit to the observed SED (hereafter $M_{\rm SED}$)· The second approach optimizes the one dimensional radial intensity profiles at selected wavelengths covering mid to far infrared bands (hereafter $M_{\rm RC}$). The radial profiles are taken along geometrically interesting axes, viz., along the line joining the two embedded sources and along lines perpendicular to the cylinder axis and passing through either of the two sources (see Fig. 4). Whereas the first approach gives precedence to the overall energetics the latter gives more importance to the structural details in the isophotes, particularly close to the embedded sources and the region between them. The actual reality may lie somewhere in between these two approaches.

The axes where radial cuts have been taken are also displayed on the 12 and 210 μm maps in Fig. 4. The fits to the observed SED for both $M_{\rm SED}$ as well as $M_{\rm RC}$ are presented in Fig. 5. Comparison of the radial cuts at 12 and 210 μm along the three axes between the observed maps and the best fit $M_{\rm RC}$ model is shown in Fig. 6.

The $M_{\rm SED}$ approach fits the observed SED very well right through near-IR to sub-mm, though there is some discrepancy in the far-IR (Fig. 5). On the other hand, fit from the $M_{\rm RC}$ approach is reasonable for $\lambda \geq 25$ μm only. The radial cuts at 210 μm fit the observed data very well. However, at 12 μm although the model predictions qualitatively agree with the data, there are discrepancies viz., the extent of emission along vertical axis and the relative contrast of the minima between the two sources. From the above it appears that the $M_{\rm RC}$ approach is very sensitive to the exact distribution of sources, specially at shorter wavelengths (which traces much hotter

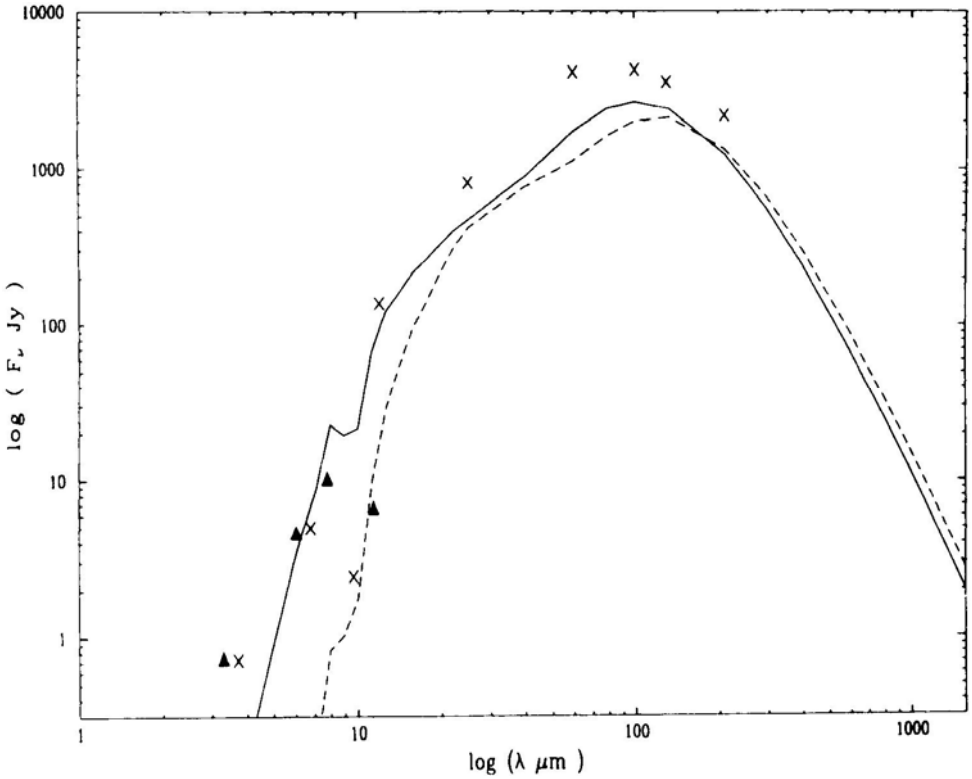

Figure 5. The SEDs for the source IRAS 19181 + 1349 predicted by the radiative transfer models. The solid and the dashed lines represent best fit models from the M_{SED} and M_{RC} approaches, respectively. The crosses represent HIRES (processed IRAS), T1FR and ISOCAM continuum flux densities. The solid triangles represent ISOCAM flux densities measured through filters centered on the PAH features.

dust and hence physically closer to the exciting source). One possibility for these discrepancies is that our model is too simplified than the actual reality in IRAS 19181 + 1349. For example there may be a distribution of sources along the line joining S1 and S2 and away from it, but with more concentration near S1 and S2. This way the discrepancy for M_{RC} in the mid-IR part of SED will also be explained. Assuming a constant dust density in the cloud may also be a major reason for the discrepancy.

The results of modelling IRAS 19181 + 1349 in the form of best fit model parameters as found under both the approaches (M_{SED} and M_{RC}) are presented in Table 1. The value of τ_{100} found from both the approaches are well within the range of validity of the code, i.e. much less than 0.06. The luminosities of both the sources are similar and the dust is found to be predominantly (80%) Silicate with no Silicon Carbide, the rest (20%) being Graphite. It is remarkable that almost all the important parameters are identical as found from both the approaches. The only difference is seen at the physical sizes of the cavities. The remarkable similar physical parameters obtained from both the approaches gives good confidence on the derived astrophysical parameters for the Galactic star forming region IRAS 19181 + 1349.

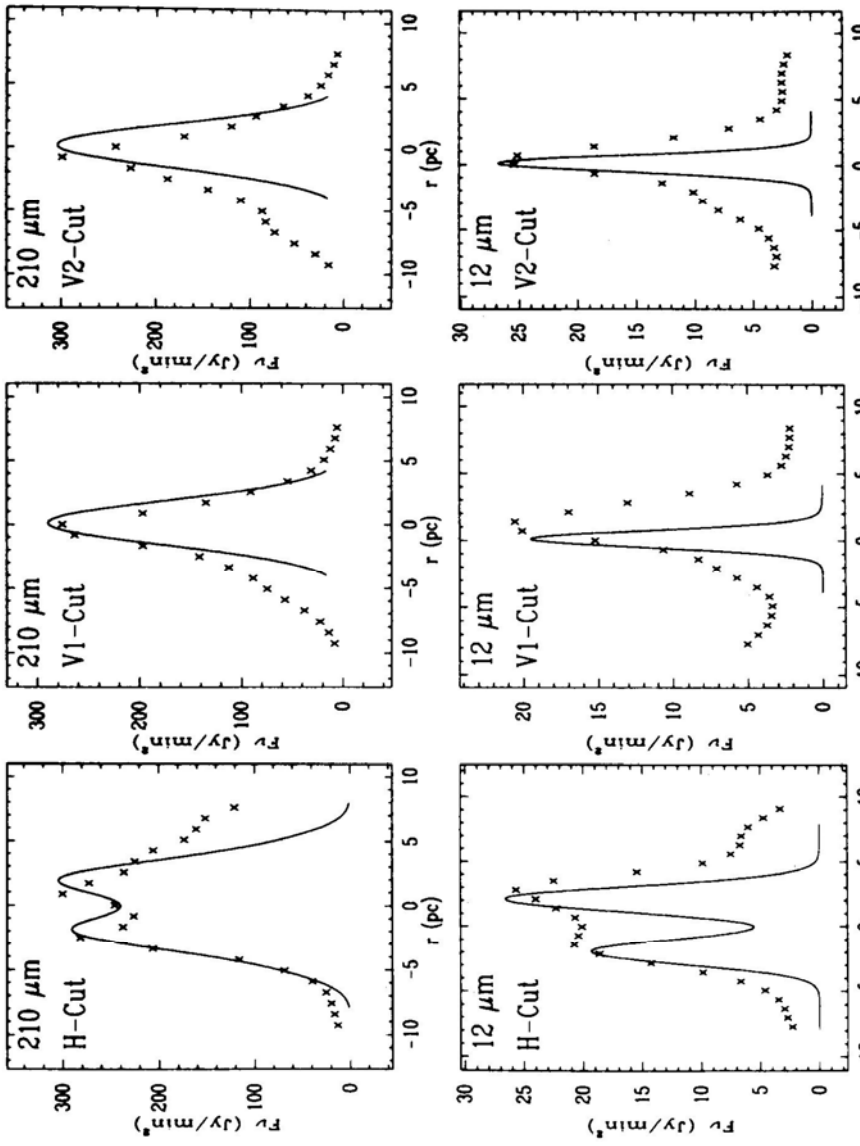

Figure 6. The axial and radial cuts predicted by the radiative transfer model (M_{RC}) (continuous lines), compared with the observations (crosses), at 12 and 210 μm. The spatial positions of the cuts are displayed in Fig. 4.

Table 1. Best fit model parameters for M_{RC} and M_{SED} schemes.

Parameter	M_{RC}	M_{SED}
R_c (pc)(Source 1)	0.11	0.03
R_c (pc)(Source 2)	0.09	0.01
$L_{source1}$ ($L_\odot$)	6.2×10^5	6.2×10^5
$L_{source2}$ ($L_\odot$)	6.3×10^5	6.3×10^5
$\tau_{100\,cyl}$ (/pc)	0.024	0.028
R_{cyl} (pc)	2.1	1.8
Graphite : Silicate : SiC	20 : 80 : 0	20 : 80 : 0

This scheme will be useful to model other similar double sources. A huge database from ISO (SEDs as well as images leading to radial cuts, covering 2.5 to 200 μm of the spectrum) will soon become available for such modelling.

4. Summary

High angular resolution mid/far infrared maps of many Galactic star forming regions show evidence for multiple embedded energy sources in the corresponding interstellar clouds. With the aim of studying such star forming regions with two embedded sources, a scheme has been developed to carry out radiative transfer calculations in a uniform density dust cloud of cylindrical geometry, and which includes the effect of isotropic scattering in addition to the absorption and emission processes. In addition to the luminosities of the two embedded energy sources, the cylindrical cloud size, separation between the two sources, dust density and composition are the parameters for the modelling. The accuracy of our scheme has been tested by comparing the results with a well established 1-D code.

An attempt was made to model the Galactic star forming region associated with IRAS 19181 + 1349 which shows double peaks in the mid- and far-infrared maps using the scheme described here. Two independent approaches were employed to find the best fit models for IRAS 19181 + 1349. Whereas the first (M_{SED}) approach aims to fit the observed SED best; the latter (M_{RC}) aims to fit the radial intensity profiles (along a few important axes) at mid-to far-infrared wavebands. Interestingly most of the crucial model parameters like luminosities, effective temperatures, dust composition, optical depth etc. turn out to be identical under both the approaches.

Acknowledgements

It is a pleasure to thank the members of the Infrared Astronomy Group of T.I.F.R. for their encouragement.

References

Egan, M. P., Leung, C.M.,SpagnaJr, G. F.,1988, *Computer Physics Communications,* **48**, 271.
Ghosh, S. K., Tandon, S. N., 1985, *Mon. Not. R. Astr. Soc.,* **215**, 315.
Karnik, A. D., Ghosh, S. K., Rengarajan, T. N., Tandon, S. N., Verma, R. P, 1999, *Bull. Astr. Soc. India*, **27**, 167.

Kurtz, S., Churchwell E., Wood, D. O. S. 1994, *Astrophys. J. Suppl.*, **91**, 659.
Laor, A., Draine, B. T., 1993, *Astrophys. J.*, **402**, 441.
Mathis, J. S., Rumpl, W., Nordsieck, K. H. 1977, *Astrophys. J.*, **217**, 425.
Rouan, D.,1979, *Astr. Astrophys.*,**79**, 102.
Verma, R. R, Ghosh, S. K., Karnik, A. D., Mookerjea, B., Rengarajan, T. N. 1999, *Bull. Astr. Soc. India,* **27**, 159.
Zoonematkermani, S., Helfand, D. J., Becker, R. H., White, R. L., Perley, R. A., 1990, *Astrophys. J. Suppl*, **74**, 181.